

pubs.acs.org/JACS Article

Quantum Gate Operations on a Spectrally Addressable Photogenerated Molecular Electron Spin-Qubit Pair

Haochuan Mao, Gediminas J. Pažėra, Ryan M. Young, Matthew D. Krzyaniak,* and Michael R. Wasielewski*



Cite This: J. Am. Chem. Soc. 2023, 145, 6585–6593



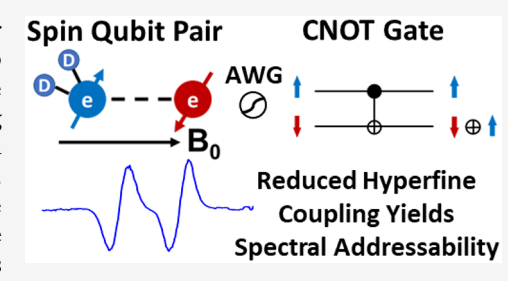
ACCESS I

III Metrics & More

Article Recommendations

s Supporting Information

ABSTRACT: Sub-nanosecond photodriven electron transfer from a molecular donor to an acceptor can be used to generate a radical pair (RP) having two entangled electron spins in a well-defined pure initial singlet quantum state to serve as a spin-qubit pair (SQP). Achieving good spin-qubit addressability is challenging because many organic radical ions have large hyperfine couplings (HFCs) in addition to significant g-anisotropy, which results in significant spectral overlap. Moreover, using radicals with g-factors that deviate significantly from that of the free electron results in difficulty generating microwave pulses with sufficiently large bandwidths to manipulate the two spins either simultaneously or selectively as is necessary to implement the controlled-NOT (CNOT) quantum gate essential for



quantum algorithms. Here, we address these issues by using a covalently linked donor–acceptor(1)–acceptor(2) (D-A₁-A₂) molecule with significantly reduced HFCs that uses fully deuterated *peri*-xanthenoxanthene (PXX) as D, naphthalenemonoimide (NMI) as A₁, and a C₆₀ derivative as A₂. Selective photoexcitation of PXX within PXX- d_9 -NMI-C₆₀ results in sub-nanosecond, two-step electron transfer to generate the long-lived PXX*- d_9 -NMI-C₆₀*- SQP. Alignment of PXX*- d_9 -NMI-C₆₀*- in the nematic liquid crystal 4-cyano-4'-(n-pentyl)biphenyl (5CB) at cryogenic temperatures results in well-resolved, narrow resonances for each electron spin. We demonstrate both single-qubit gate and two-qubit CNOT gate operations using both selective and nonselective Gaussian-shaped microwave pulses and broadband spectral detection of the spin states following the gate operations.

■ INTRODUCTION

New computation, communication, and sensing technologies provided by quantum information science (QIS) are drawing considerable attention.^{1–3} The identification and characterization of new molecular systems to serve as qubits in these applications have motivated chemists to contribute to this field^{4,5} by taking advantage of synthetic tunability^{6,7} and the ease with which unpaired electron spins in molecules can be manipulated using microwave pulses.^{8–10} These molecular systems employ multiple electron spin qubits within interacting organic radicals^{8,9,11–14} and/or metal complexes^{15–20} and have achieved advances in extending coherence lifetimes^{17,21,22} and scaling up the number of qubits.^{18,23–25} However, thermally polarized electron spins²⁶ with well-defined initial spin states essential for QIS applications²⁷ are only available at high magnetic fields and/or millikelvin temperatures.¹¹

Spin-selective, light-driven processes in molecular qubit systems have shown significant promise for creating well-defined initial electron spin-qubit states. 4,20,28-30 For example, sub-nanosecond photodriven electron transfer from a molecular donor (D) covalently linked to an acceptor (A) via a bridge molecule (B) has been shown to generate a D*+B-A*-radical pair having two entangled electron spins in a well-defined pure initial singlet quantum state that can serve as a spin-qubit pair (SQP) even at room temperature. 28,31,32 The

entanglement of the two electron spins in these SQPs results from their electron spin-spin exchange (J) and/or dipolar (D)couplings. In addition, the two electron spins of the SQP experience different magnetic environments as a consequence of differing electron-nuclear hyperfine couplings (HFCs) between D⁺⁺ and A⁺⁻, as well as differing spin-orbit interactions within each radical ion leading to different electronic g-tensors. The two-particle wave functions of the SQP in the coupled basis are $|S\rangle$, $|T_{+1}\rangle$, $|T_0\rangle$, and $|T_{+1}\rangle$, where $|S\rangle = 1/\sqrt{2} [|\alpha\beta\rangle - |\beta\alpha\rangle]$ and $|T_0\rangle = 1/\sqrt{2} [|\alpha\beta\rangle + |\beta\alpha\rangle]$ constitute two of the four possible entangled Bell states of the system.³³ The other two Bell states, $1/\sqrt{2} \left[|\alpha\alpha\rangle + |\beta\beta\rangle \right]$ and $1/\sqrt{2} [|\alpha\alpha\rangle - |\beta\beta\rangle]$, are obtained by linear combinations of $|T_{+1}\rangle = |\alpha\alpha\rangle$ and $|T_{-1}\rangle = |\beta\beta\rangle$. Upon application of a magnetic field that is much larger than J, D, and the differences in the HFCs and g-tensors of both radical ions comprising the SQP, only the $|S\rangle$ and $|T_0\rangle$ spin states of the SQP are close in

Received: February 2, 2023 Published: March 13, 2023





energy and mix to give $|\Phi_A\rangle$ and $|\Phi_B\rangle$ (Figure 1). These mixed states are described by $|\Phi_A\rangle = \cos\phi |S\rangle + \sin\phi |T_0\rangle$ and $|\Phi_B\rangle$

$$\ket{\Phi_{\mathrm{B}}}$$
 $\ket{\Phi_{\mathrm{A}}}$ $\ket{\Phi_{\mathrm{A}}}$

Figure 1. Radical pair energy levels in the high magnetic field limit showing the result of mixing $|S\rangle$ and $|T_0\rangle$ states.

= $\cos\phi |T_0\rangle + \sin\phi |S\rangle$, where the angle ϕ describes the degree of mixing and is related to J, D, and the differences in the HFCs and g-tensors of the two radical ions. In contrast, the $|T_{+1}\rangle$ and $|T_{-1}\rangle$ states are energetically far removed from $|T_0\rangle$ and do not mix with $|S\rangle$. Since the SQP is initially formed in a pure $|S\rangle$ state, $|\Phi_A\rangle$ and $|\Phi_B\rangle$ are overpopulated, which produces strong spin polarization that can be observed readily with time-resolved EPR spectroscopy using either continuous (TREPR) or pulsed microwave radiation (pulse-EPR).

Pulse-EPR has been used to demonstrate quantum state teleportation, ¹² spin polarization transfer to a third spin, ^{39–42} and varying degrees of qubit-specific addressability using photogenerated SQPs. ^{14,43} However, the radical ions employed in these D-B-A molecules typically have large hydrogen and nitrogen HFCs relative to the difference in their g-tensors, which results in significant spectral overlap of the two spin resonances of the SQP, limiting spectral resolution and thus addressability. In addition, a distribution of the D•+ and A•- g-tensor orientations relative to one another and to the applied magnetic field often contributes to spectral broadening. All of these effects make it difficult to generate microwave pulses with sufficiently broad bandwidths to manipulate the two spins of the SQP either simultaneously or selectively as is necessary to implement the controlled-NOT (CNOT) quantum gate essential for executing quantum algorithms. ^{13,44}

1: PXX-NMI-C₆₀; 1-d₉: PXX-d₉-NMI-C₆₀

Here, we address these issues by designing and synthesizing a covalently linked donor—acceptor(1)—acceptor(2) (D-A₁-A₂) molecule with significantly reduced HFCs by using fully deuterated *peri*-xanthenoxanthene (PXX) as D, naphthalenemonoimide (NMI) as A₁, and a C₆₀ derivative as A₂ (1-d₉). These donors and acceptors were chosen to optimize the photoinduced electron transfer rates within PXX-d₉-NMI-C₆₀ to ensure rapid two-step electron transfer leading to PXX**-d₉-NMI-C₆₀*- at cryogenic temperatures. PXX has a lowest excited singlet state energy $E_{\rm s}=2.75$ eV; yet it is relatively easy to oxidize ($E_{\rm ox}=0.82$ V vs SCE^{45,46}). NMI was chosen as the intermediate acceptor because it does not absorb in the visible

spectrum, and its one-electron reduction potential is sufficiently negative ($E_{\rm RED}=-1.4~{\rm V}~{\rm vs}~{\rm SCE}^{47}$) to ensure that the energy of the initial photogenerated SQP PXX*-- d_9 -NMI*-- C_{60} is high enough to rapidly reduce C_{60} ($E_{\rm red}=-0.6~{\rm V}~{\rm vs}~{\rm SCE}^{48}$) to give PXX*-- d_9 -NMI- C_{60} *-.

Selective photoexcitation of PXX within PXX- d_9 -NMI-C₆₀ results in sub-nanosecond, two-step electron transfer to form an entangled, long-lived PXX*-NMI-C₆₀*- SQP. Alignment of PXX*-NMI-C₆₀*- in the nematic liquid crystal 4-cyano-4'-(n-pentyl)biphenyl (5CB) effectively eliminates the spectral complexities resulting from the anisotropic g-tensors of both PXX*- and C₆₀*-, which results in well-resolved resonances for each electron spin, thus providing a platform for quantum gate operations. We demonstrate both single-qubit gates and two-qubit CNOT gates implemented with frequency-selective and broadband, nonselective Gaussian-shaped microwave pulses followed by broadband spectral detection of the spin states following the gate operations.

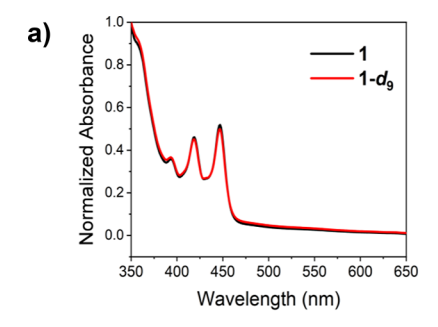
EXPERIMENTAL METHODS

Synthesis. Detailed synthetic procedures and characterization of 1 and 1- d_9 are given in the Supporting Information (SI). The PXX radical cation (PXX*-1) and PXX- d_{10} radical cation (PXX*-10) were prepared by adding a substoichiometric amount (0.8 equiv) of nitrosonium tetrafluoroborate to a 100 μ M dichloromethane solution of PXX or PXX- d_{10} , respectively. The radical solutions were used immediately for EPR measurements.

Optical Spectroscopy. UV-visible absorption spectra were obtained using a Shimadzu UV-1800 spectrometer in a quartz cuvette with a 1 mm path length. Femtosecond and nanosecond transient absorption (fsTA and nsTA) spectroscopy was conducted using an apparatus described previously (for a brief description see the SI).⁴⁹ Samples for room-temperature TA experiments were dissolved in toluene and prepared with an optical density of 0.8 at 450 nm in 2 mm quartz cuvettes fused to a glass bulb. This bulb was used to subject each sample to four freeze-pump-thaw cycles under vacuum (10⁻⁴ Torr) to remove oxygen. Samples were stirred to minimize the effects of local heating and degradation. For TA experiments at low temperature, a solution of 1 in CH₂Cl₂ was prepared with an optical density of 0.8 at 450 nm in a 2 mm quartz cuvette. The solution was then evaporated to dryness with a stream of N₂ in a small vial and was placed in a N2-atmosphere glovebox. Inside the glovebox, a volume of 2-methyltetrahydrofuran (mTHF) equivalent to the amount of CH2Cl2 used previously was added to the vial to obtain a solution of similar optical density. This solution was then sealed in a sample cell consisting of two quartz windows separated by a 2 mm PTFE spacer. The sealed sample cell was then removed from the glovebox and placed inside a Janis VNF-100 cryostat (Janis Research Co. LLC) coupled to a Cryo-Con 32B (Cryogenics Control Systems, Inc.) temperature controller. The sample was then cooled to 85 K to measure the TA spectra.

Visible and near-infrared data were individually chirp-corrected (Surface Xplorer 4, Ultrafast Systems, LLC), and fsTA and nsTA data were merged in MATLAB prior to kinetic analysis. Data were analyzed using selected-wavelength global fitting to the models as described in the text. The errors of the lifetimes given in the figures are derived from the standard deviations from the global fitting propagated with the uncertainty described by the instrument response (0.3 ps and 0.8 ns for fsTA and nsTA, respectively). Details of the kinetic fitting were described previously. ⁵⁰

Steady-State Continuous-Wave EPR Spectroscopy (CW-EPR). CW-EPR measurements were performed on ~20 μ L, 100 μ M samples in dichloromethane solution that were loaded into quartz tubes (2.40 mm o.d., 2.00 mm i.d.), subjected to three freeze-pump-thaw cycles on a vacuum line (10⁻⁴ Torr), and sealed with a hydrogen torch. Measurements at the X-band (9.5 GHz) were performed with a Bruker Elexsys E580, equipped with a 4122SHQE resonator. Scans were performed with a magnetic field modulation amplitude of 0.1 G,



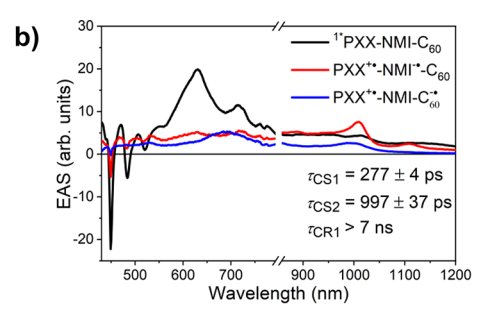


Figure 2. (a) UV-vis spectra of 1 and 1- d_9 in toluene solution at 295 K. (b) Evolution-associated spectra obtained from fsTA data of 1 at 85 K in mTHF solution following $\lambda_{ex} = 450$ nm excitation.

modulation frequency of 60 kHz, and nonsaturating microwave power of 1.5 mW. $\,$

Time-Resolved EPR Spectroscopy. Measurements were made at the X-band (~9.6 GHz) on a Bruker Elexsys E680 X/W EPR spectrometer with a split ring resonator (ER4118X-MS3). The temperature was set by an Oxford Instruments CF935 continuous flow optical cryostat with liquid nitrogen or liquid helium. Direct detection using CW microwaves was performed following photoexcitation. Kinetic traces of the transient magnetization under CW microwave irradiation were detected in quadrature. Time traces were recorded over a range of magnetic fields to give 2D spectra. Spectra were processed by first subtracting the signal prior to the laser pulse for each kinetic trace (at a given magnetic field point) and then subtracting the signal average at off-resonant magnetic field points from the spectra obtained at a given time. All processing and fitting of the spectra were performed in MATLAB using lab-written scripts and the simulation package EasySpin v6.0-dev. ⁵¹

Pulse-EPR Spectroscopy. Shaped microwave pulses were generated using a commercial Bruker SpinJet II arbitrary waveform generator (AWG) module. A Gaussian-shaped pulse was used for both selective and nonselective turning angle operations because it provides a more uniform excitation across the field-swept echodetected spectrum than traditional square pulses. The excitation profiles of 20 and 80 ns Gaussian pulses were measured to provide sufficient bandwidth for the nonselective and selective SQP excitations, respectively, necessary to perform the CNOT gate pulse sequence (Figure S1). The turning angles of these pulses were controlled by their amplitude as output by the AWG. These amplitudes were kept within a linear response regime of the traveling wave tube (TWT) amplifier. The resonator response profile (Figure S2) and the TWT response profile and amplitude for the pulse turning angles for specific pulse lengths were calibrated with the EPR signal from the triplet state of C_{60} as an internal standard generated by photoexcitation of the sample. All of the pulse experiments were started with an initial delay after the laser flash $T_{DAF} = 50$ ns. The electron spin echoes were collected with a $\pi/2-\tau-\pi$ pulse sequence, with $\tau = 500$ ns, and a 16-step CYCLOPS⁵² phase cycle; this tau value was chosen to ensure that the spin-echo was not truncated by the instrument deadtime and to be well within the $T_{\rm m}$ = 1.5 μs phase memory time of PXX*+-d9-NMI-C60*- (Figure S7). Prior to Fourier transformation, the echo was apodized with a Hamming window, zero-filled, and circularly shifted to evenly split the spin-echo. Following Fourier transformation, the spectrum was appropriately phased into absorption/emission and dispersion. In the single-qubit nutation experiment, the variable amplitude nutation pulse occurred 500 ns before the detection sequence.

RESULTS AND DISCUSSION

Optical Spectroscopy. Steady-state absorption spectra of 1 and $1-d_9$ in toluene are shown in Figure 2a. Since deuteration does not change the electronic structure of PXX, 1 and $1-d_9$ have identical absorption spectra with a characteristic vibrational progression at 393, 417, and 447 nm resulting from

PXX.^{45,46} The strong absorption below 360 nm and broad absorption that covers the entire visible region with stronger absorption at shorter wavelengths results from C_{60} .^{53,54}

Transient absorption spectroscopy was used to monitor the photoinduced electron transfer dynamics of 1 in 2-methyltetrahydrofuran (mTHF) at 85 K. Time-resolved spectra at selected times and kinetic fits at selected wavelengths are shown in Figure S3, while global fitting of the data set using an $A \rightarrow B \rightarrow C$ model yields the evolution-associated spectra given in Figure 2b. Immediately after laser excitation of PXX in 1, a ground-state bleach appears at 450 nm along with stimulated emission features at 480 and 520 nm and an excited-state absorption at 650 nm. The subsequent charge transfer reaction $^{1}*PXX-NMI-C_{60} \rightarrow PXX^{\bullet+}-NMI^{\bullet-}-C_{60}$ occurs in $\tau_{\rm CS1}$ = 277 ± 4 ps, resulting in the appearance of absorption bands at 530 and 1000 nm due to PXX*+.45,46 The second charge transfer reaction, PXX*+-NMI*-- $C_{60} \rightarrow PXX^{\bullet+}$ -NMI- C_{60} , occurs in $\tau_{CS2} = 997 \pm 31$ ps, as evidenced by broadening of the 1000 nm absorption peak due to the coexistence of $C_{60}^{\bullet-}$ and PXX.*+. PXX.*+-NMI- $C_{60}^{\bullet-}$ eventually decays to form PXX-NMI- $^{3*}C_{60}$ with a time constant of 2.0 \pm 0.2 μ s (Figure S4). As will be shown below, lowering the temperature to 10 K results in increasing this lifetime to 13 \pm 1 μ s. Partial coexcitation of C₆₀ also produces some C₆₀ triplet excited state (3*C₆₀), which has an absorption at 680 nm that appears on a longer time scale (Figure S4).

CW-EPR Spectroscopy. Chemically generated PXX* and PXX*- d_{10} in dichloromethane solution were characterized by CW-EPR spectroscopy (Figure S5). The unpaired electron in PXX*- is coupled to its hydrogen atoms, and the isotropic hyperfine coupling constants (HFCs) of the five inequivalent hydrogen atoms were obtained from fitting the experimental spectrum and are summarized in Table S1. The EPR spectrum of PXX*- d_{10} exhibits significant spectral narrowing resulting from the d_{10} -6.5-fold reduction in gyromagnetic ratio of deuterium relative to hydrogen. The structure that appears atop the derivative spectrum of PXX*- d_{10} results from unresolved deuterium HFCs.

TREPR Spectroscopy. To evaluate the feasibility of $PXX^{\bullet+}$ - d_9 -NMI- $C_{60}^{\bullet-}$ as a potential SQP system for quantum gate operations, TREPR measurements were performed on both 1 and 1- d_9 in mTHF and 5CB at 85 K. The spectra were recorded in direct detection mode, where positive signals are enhanced absorptive (a) transitions and negative signals are emissive (e) ones. Figure 3 shows the corresponding TREPR spectra at 200 ns after a 7 ns, 450 nm laser pulse. The difference in g-tensors between PXX $^{\bullet+}$ and $C_{60}^{\bullet-}$ allows for spectral separation of the two radicals at X-band frequencies. However, significant line broadening at lower field was

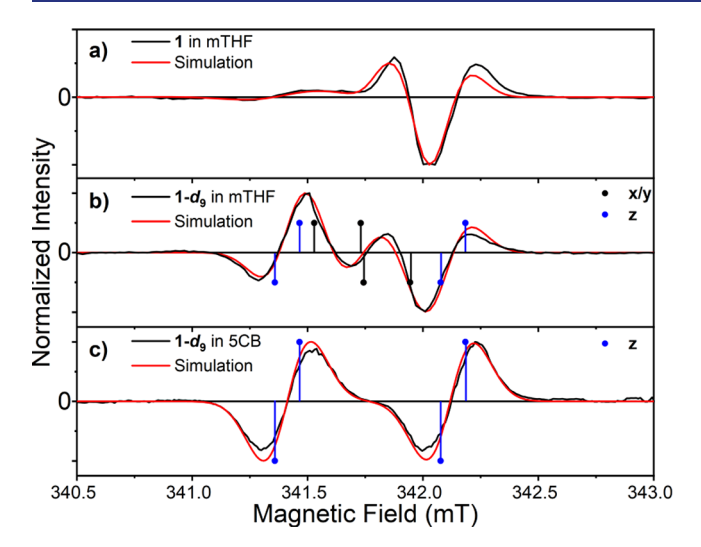


Figure 3. TREPR spectra at 85 K and 200 ns following a 450 nm, 7 ns laser pulse and spectral simulations. (a) $PXX^{\bullet+}$ -NMI- $C_{60}^{\bullet-}$ (1) in mTHF, (b) $PXX-d_9^{\bullet+}$ -NMI- $C_{60}^{\bullet-}$ (1- d_9) in mTHF, and (c) $PXX-d_9^{\bullet+}$ -NMI- $C_{60}^{\bullet-}$ (1- d_9) in 5CB aligned along the magnetic field. The vertical lines connected to the dots show the transitions of the SQPs, whose principal axes, x, y or z, are parallel to the magnetic field, where z is defined as the direction that connects the two spins, and x and y are perpendicular to z.

observed for 1 due to the unresolved hydrogen atom HFCs in PXX $^{\bullet+}$ (Figure 3a). The higher field portion of the spectrum with transitions primarily from $C_{60}^{\bullet-}$ has a narrow (a,e,a) polarization pattern owing to the nuclear-spin-free nature of $C_{60}^{\bullet-}$ and its axial g-tensor, whose anisotropy is likely due to the pyrrolidino-functionalization of C_{60} that distorts its symmetry.

Compared to 1, the lower field features in the TREPR spectrum of $1-d_9$ in mTHF are narrowed in the absence of hydrogen HFCs. The entire TREPR spectrum of $1-d_9$ is nearly centrosymmetric and shows an (e,a,e,a,e,a) polarization pattern,

which deviates from the ideal (e,a,e,a) pattern predicted for the four spin transitions of SQPs. This deviation is attributed to the axial g-tensors of both PXX*+ and C_{60} *-. The Zeeman splitting of an electron spin in an anisotropic molecule is a function of the molecular orientation with respect to the external magnetic field; likewise, the TREPR spectrum of a randomly oriented ensemble of SQPs in a frozen matrix, such as that of 1- d_9 in mTHF, results in a powder pattern composed of the SQP transitions at all orientations (Figure 3b).

To eliminate the spectral complexity from random molecular orientations, $1\text{-}d_9$ was dissolved in 5CB, and the sample was aligned by the magnetic field at 295 K, then frozen. The aligned sample shows a well-resolved (e,a,e,a) polarization pattern (from lower field to higher field) spanning roughly 35 MHz that permits qubit addressability using both frequency-selective and nonselective microwave pulses necessary for quantum gate operations (Figure 3c). The TREPR spectra of 1 and $1\text{-}d_9$ can be globally simulated using the same spin model with a spin–spin dipolar coupling constant D=-3 MHz and two axial g-tensors:, [2.0045, 2.0045, 2.0031] and [2.0003, 2.0003, 2.0019], for PXX** and C_{60} ** respectively. The spectral simulation of 1 in frozen mTHF used a 20 MHz Gaussian peak-to-peak line width to account for unresolved hydrogen HFCs of PXX** (Table S1).

EPR Spectral Readout with Nonselective Pulses. The strategies of g-factor engineering, deuteration, and alignment of 1-d₉ produce well-resolved SQP EPR spectra, allowing for uniform excitation of the entire EPR spectrum using a 20 ns Gaussian-shaped microwave pulse. Instead of using traditional field-sweep detection, the EPR spectrum of 1-d₉ in 5CB in the frequency domain can be obtained by measuring the entire spin—echo time trace in the time domain⁵⁶ at the central magnetic field of the spectrum and performing a Fourier transform to obtain the EPR spectrum in the frequency domain. In principle, when all the spin transitions are excited, the resulting frequency spectrum of the SQP should exhibit the same spectral features and polarization pattern as the TREPR spectrum. To ensure the same bandwidths between the two

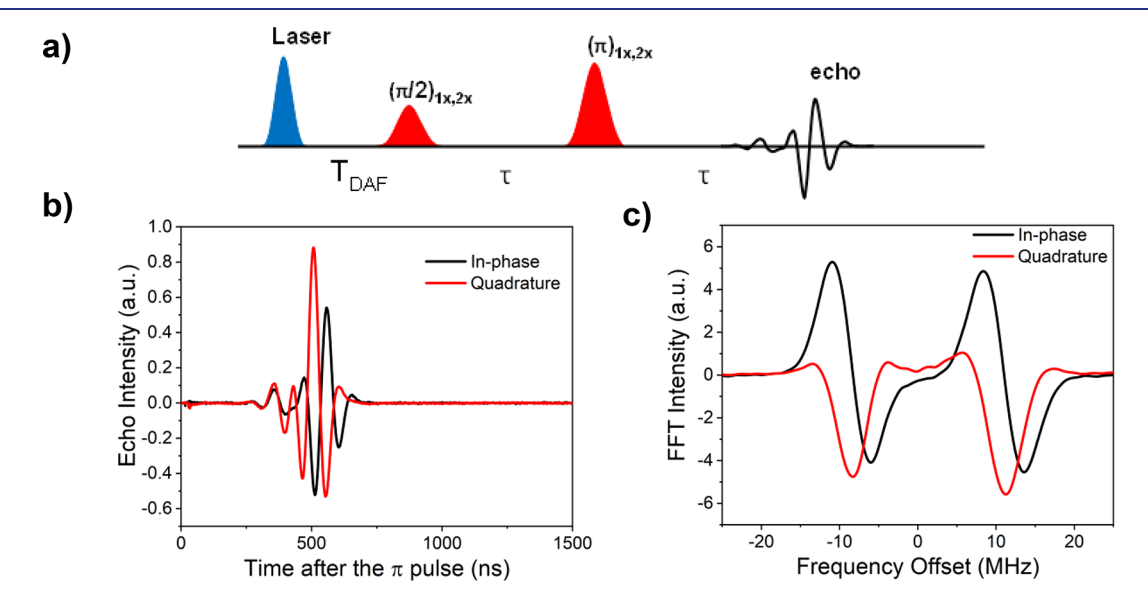


Figure 4. (a) Pulse sequence used to measure the EPR spectrum of PXX- $d_9^{\bullet^+}$ -NMI- $C_{60}^{\bullet^-}$ (1- d_9) at 85 K in aligned 5CB, where $T_{\rm DAF}=50$ ns, $\tau=500$ ns, and variable amplitude 20 ns microwave pulses were used to produce the $\pi/2$ and π turning angles as described in the text. (b) Spin echo of PXX- $d_9^{\bullet^+}$ -NMI- $C_{60}^{\bullet^-}$ showing oscillatory behavior due to the structure of the frequency spectrum. Both the in-phase and quadrature parts of the signal were collected. (c) The frequency domain spectrum of the spin echo showing both $C_{60}^{\bullet^-}$ and PXX- $d_9^{\bullet^+}$, from low to high frequency.

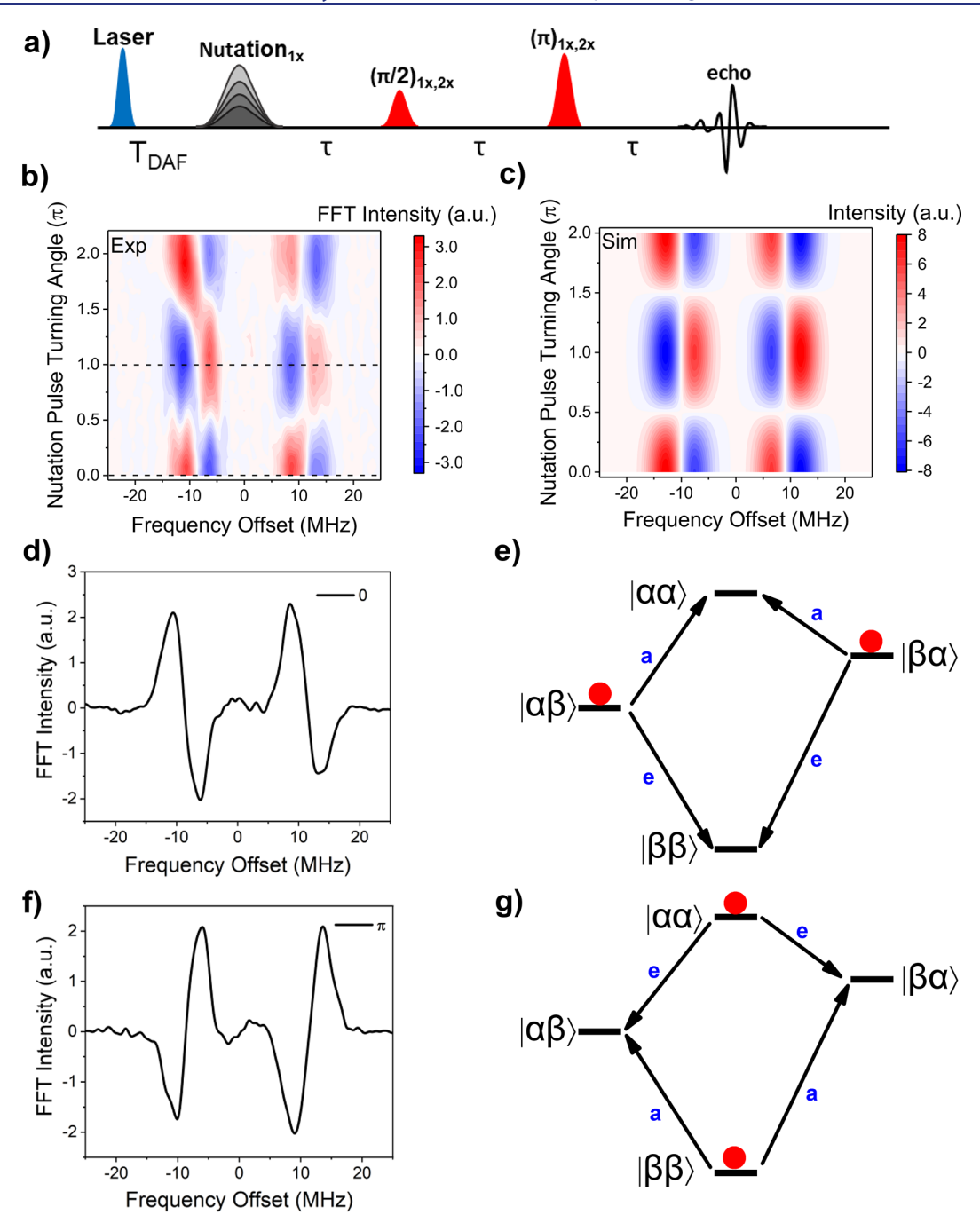


Figure 5. (a) Pulse sequence of the single-qubit nutation where $T_{\rm DAF}=50$ ns, the black pulse is a frequency-selective 80 ns nutation pulse, $\tau=500$ ns, and the red pulses are 20 ns frequency-nonselective $\pi/2$ and π readout pulses. (b) Frequency spectra after a single-qubit nutation pulse on $C_{60}^{\bullet-}$ within PXX- $d_9^{\bullet+}$ -NMI- $C_{60}^{\bullet-}$ (1- d_9) at 10 K. (c) Frequency space simulation of the effect of a single-qubit pulse with varying turning angles. (d and f) Spectral slices at the dashed lines in (b), where the turning angles of the selective nutation pulses are 0 and π , respectively. (e and g) Spin level population diagrams for selective nutation pulses 0 and π , respectively, applied to $C_{60}^{\bullet-}$.

pulses, the turning angles of the $\pi/2$ and π microwave pulses were determined by adjusting the pulse amplitudes rather than the pulse lengths (Figure 4a). The SQP spin—echo shows strong oscillations (Figure 4b), which carry all the spectral information in the time domain, similar to a free induction decay (FID). The TREPR spectrum of 1- d_9 in 5CB is well-reproduced in the frequency domain (Figure 4c), showing the same (e,a,e,a) polarization pattern (from high frequency to low frequency), which demonstrates this technique as a feasible detection scheme for quantum gate operations.

Single-Qubit Operations. Single-qubit operations were performed on 1- d_9 oriented in 5CB at 10 K using an 80 ns Gaussian-shaped, frequency-selective pulse. Decreasing the temperature from 85 K to 10 K extends the SQP lifetime from $2.0 \pm 0.2 \, \mu s$ to $13 \pm 1 \, \mu s$ (Figure S6). The amplitude of this pulse was incremented to perform a nutation that targeted either $C_{60}^{\bullet-}$ or PXX $^{\bullet+}$, depending on the frequency offset of the pulse (Figure S1b). The effect of the single-qubit nutation pulse was monitored using the detection scheme discussed in the previous section. Figure 5a shows the pulse sequence used in this experiment, where the nutation pulse has a frequency

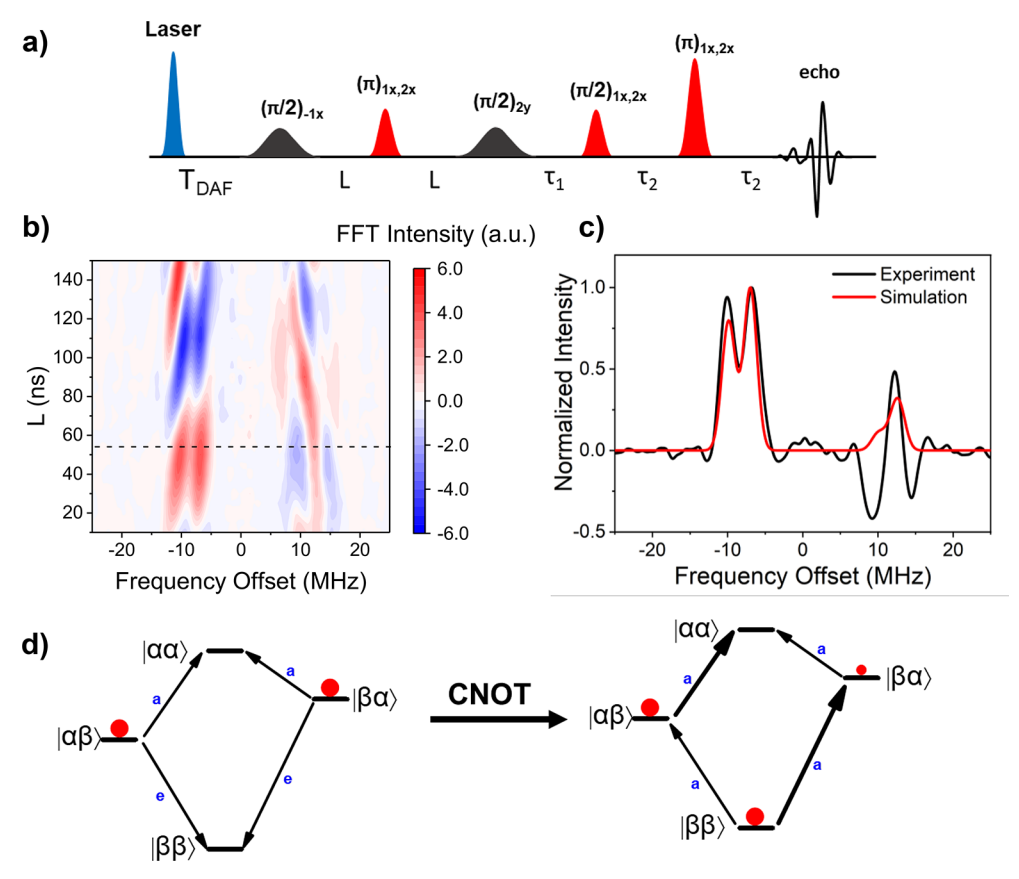
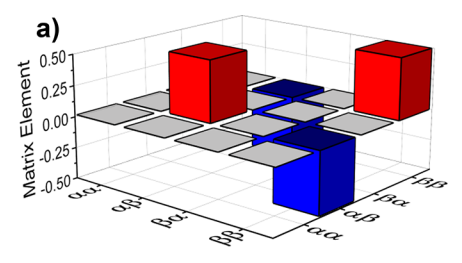


Figure 6. (a) Pulse sequence for CNOT gate and detection, where $T_{\rm DAF}=50$ ns. The two frequency-selective 80 ns pulses (black), the variable time delay L, and the first 20 ns frequency-nonselective pulse (red) constitute the CNOT gate. This is followed by two 20 ns frequency-nonselective $\pi/2$ and π readout pulses (red), where $\tau_1=200$ ns, $\tau_2=500$ ns. The frequency spectrum after the three-pulse CNOT gate operation with incremental L is plotted in (b) using PXX*+ as the control qubit at 10 K. The slice marked by the dashed line in (b) is shown in (c), and simulation is shown in red. (d) Spin level population diagrams of the SQP before and after the CNOT gate.

offset of -9 MHz that selectively operates on $C_{60}^{\bullet-}$. The frequency spectrum of the SQP produced after photoexciting $1-d_9$ is plotted against the turning angle of the nutation pulse in Figure 5b, which can be simulated accurately in the frequency domain, Figure 5c. In addition, if PXX*+ is selectively excited by the nutation pulse, the same nutation behavior is observed (Figure S8a), which can also be simulated accurately (Figure S8b). This nutation effect is attributed to entanglement between the $C_{60}^{\bullet-}$ and PXX $^{\bullet+}$ electron spins. ⁴⁴ The PXX $^{\bullet+}$ d_9 -NMI-C₆₀ - SQP generated after photoexciting 1- d_9 is in an initial singlet state, which results in population of the $|\alpha\beta\rangle$ and $|\beta\alpha\rangle$ spin states of the SQP in the high field limit⁵⁷ (Figure 5d), where the first and second Greek letters in the kets denote the spin states of PXX $^{\bullet+}$ and $C_{60}^{\bullet-}$, respectively. The absorptive and emissive spectral features of C₆₀ • are assigned to the $|\alpha\beta\rangle$ to $|\alpha\alpha\rangle$ and $|\beta\alpha\rangle$ to $|\beta\beta\rangle$ transitions, respectively (Figure 5e). The spin configurations in the uncoupled basis are shown next to the energy levels to highlight the spin flips associated with each transition. The nutation π pulse applied to the transitions of $C_{60}^{\bullet-}$ acts as a NOT gate and flips the spin populations from $|\alpha\beta\rangle$ to $|\alpha\alpha\rangle$ and from $|\beta\alpha\rangle$ to $|\beta\beta\rangle$ simultaneously (Figure 5g), causing the entire spectrum to flip accordingly (Figure 5f). More generally this operation can be written as $1/\sqrt{2}[|\alpha\beta\rangle - |\beta\alpha\rangle] \xrightarrow{\text{NOT}} 1/\sqrt{2}[|\alpha\alpha\rangle - |\beta\beta\rangle]$ and is a protocol related to superdense coding in QIS.⁴⁴ The same behavior was observed when the nutation pulse was

applied to PXX^{•+}, where $1/\sqrt{2}[|\alpha\beta\rangle - |\beta\alpha\rangle] \xrightarrow{\text{NOT}} 1/\sqrt{2}[|\beta\beta\rangle - |\alpha\alpha]\rangle$, (Figure S8).

The Three-Pulse CNOT Gate. One of the original microwave pulse sequences proposed by Volkov and Salikhov⁵⁸ for the CNOT gate is composed of five microwave pulses, resulting in a relatively long gate execution time. 13 However, the fact that the photogenerated SQP is created in an initial singlet state allows for reduction of the number of pulses necessary to implement the CNOT gate (see SI, eqs S1-S4). Here, a three-pulse sequence is used to execute the CNOT gate and the spectrum after the gate is read out using a broadband Hahn echo pulse sequence as described previously (Figure 6a). 13 The CNOT gate pulse sequence comprises two 80 ns frequency-selective $\pi/2$ microwave pulses at the resonance frequencies of the control and target qubits and one 20 ns frequency nonselective π pulse that excites all four transitions of the SQP. The two spin evolution times $L = \pi/(2J)$ -8/3D), where the spin-spin exchange coupling (J) and dipolar coupling (D) between the two spins of the SQP are determined experimentally using out-of-phase electron spin echo envelope modulation measurements (OOP-ESEEM) (Figure S9). 57,59,60 Figure 6b shows the spectral changes that occur when L is incremented with $PXX^{\bullet+}$ acting as the control qubit. The SQP spectra after the pulse sequence oscillate at the same period as the OOP-ESEEM signal (Figure S9), suggesting that both J and D are contributing to the spin precession in the absence of microwave pulses. Furthermore,



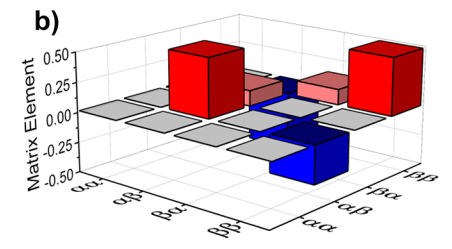


Figure 7. Expected (a) and experimentally measured (b) density matrices of the PXX- $d_9^{\bullet+}$ -NMI- $C_{60}^{\bullet-}$ (1- d_9) SQP after applying the CNOT gate.

when L = 55 ns, the CNOT gate occurs, yielding an EPR spectrum with a strong absorptive doublet (a,a) feature on resonance with $C_{60}^{\bullet-}$ and a weaker (*e,a,e*) feature on resonance with PXX^{•+} (Figure 6c). Ideally, when PXX^{•+} is acting as the control qubit, the target qubit C₆₀ - will experience a spin flip only when PXX $^{\bullet+}$ is in the β state. Therefore, when the CNOT gate is applied to the SQP with its initial spin state of $1/\sqrt{2} [|\alpha\beta\rangle - |\beta\alpha\rangle]$, the $|\alpha\beta\rangle$ state remains unchanged, whereas the $|\beta\alpha\rangle$ state is transferred to the $|\beta\beta\rangle$ state as a result of the spin flip on the target qubit because the control qubit is in the β state, $1/\sqrt{2} \left[|\alpha\beta\rangle - |\beta\alpha\rangle \right] \xrightarrow{\text{CNOT}} 1/\sqrt{2} \left[|\alpha\beta\rangle - |\beta\alpha\rangle \right]$ $|\beta\beta\rangle$]. Realistically, the $|\beta\alpha\rangle$ state in SQP is mixed with a small percentage of $|\alpha\beta\rangle$ character, thus leaving a small $|\beta\alpha\rangle$ spin population. As a consequence, applying the CNOT gate to the SQP results in an EPR spectrum with a strong absorptive doublet on the target qubit and a weaker absorption on the control qubit (Figure 6d). Once again, the spin configurations in the uncoupled basis are shown next to the energy levels to highlight the spin flips associated with each transition. However, the EPR spectrum after the CNOT gate does not completely match what is predicted by the simulation, indicating a nonunity fidelity of the CNOT gate, which is likely due to nonideality of the microwave pulses, such as the finite pulse length resulting in nonuniform excitation profiles over the desired frequency range.

Quantum State Tomography and CNOT Gate Fidelity. The fidelity F of a quantum operation as defined in eq 1 is a common metric used to assess the success of an experimental quantum logic gate, which compares an ideal density matrix ρ of a quantum system to the experimentally determined density matrix σ of the same system.

$$F(\rho, \sigma) \equiv (\operatorname{tr}\sqrt{\rho^{1/2}\sigma\rho^{1/2}})^2 \tag{1}$$

The ideal density matrix ρ can be constructed using the density matrix of the initial SQP spin state and the matrix representation of the CNOT gate. After applying the CNOT gate, the experimental density matrix σ of the SQP can be measured using frequency-selective microwave pulses with 90° turning angles (Figure S10). Using the symbols I, X, and Y to represent the identity operation, a 90° rotation about the α axis, and a 90° rotation about the y-axis, respectively, performing a total of nine operations following the CNOT gate, 61,62 II, XI, YI, IX, IY, XX, YY, XY, YX, rotates the offdiagonal elements of the density matrix to the diagonal of the matrix, which are read out as spin populations that manifest themselves as different polarization patterns in the EPR spectra (Figure S11). The experimental density matrix is reconstructed subsequently by solving linear equations whose unknowns are the matrix elements. The linear equations are simplified further by neglecting the double-quantum coherences and the coherences related to the $|\alpha\alpha\rangle$ spin state because no spin

population is present in that state. The ideal and experimental density matrices reconstructed by this method are shown in Figure 7 and eqs S14 and S15. We obtained a fidelity of 0.89, which shows that the microwave pulse sequence used here accurately executes the CNOT gate. By comparing Figures 7a and 7b, the main source of deviation from the ideal CNOT gate comes from coherence between the $|\beta\alpha\rangle$ and $|\beta\beta\rangle$ states potentially generated by nonideal excitation by the microwave pulses.

CONCLUSIONS

In this study, we synthesized PXX-d₉-NMI-C₆₀ in which deuteration of the PXX donor, use of the C₆₀ as the nuclear spin-free acceptor with an unusually low g-factor, and alignment of photogenerated PXX^{•+}-d₉-NMI-C₆₀^{•-} in 5CB result in an SQP having four spectrally separated, narrow transitions, providing a platform for quantum logic gate operations. Single-qubit gates and the two-qubit CNOT gate were demonstrated using this system, which form a complete set of gates necessary for quantum information applications. These results illustrate the opportunities afforded by tailoring the properties of photogenerated radical pairs to serve as SQPs. Nevertheless, several challenges remain in scaling-up these systems to multiqubit assemblies needed for QIS applications. Some of these challenges currently being researched include using shaped microwave pulses to establish uniform pulse bandwidths, improved gate fidelities, optical selectivity to address different SQPs, and better control of anisotropic magnetic interactions to enhance spin addressability.

ASSOCIATED CONTENT

Supporting Information

The Supporting Information is available free of charge at https://pubs.acs.org/doi/10.1021/jacs.3c01243.

Experimental details, including synthesis, NMR, mass spec, TA spectra and kinetics, and additional EPR spectra (PDF)

AUTHOR INFORMATION

Corresponding Authors

Michael R. Wasielewski — Department of Chemistry, Center for Molecular Quantum Transduction, and Institute for Sustainability and Energy at Northwestern, Northwestern University, Evanston, Illinois 60208-3113, United States; orcid.org/0000-0003-2920-5440; Email: m-wasielewski@northwestern.edu

Matthew D. Krzyaniak – Department of Chemistry, Center for Molecular Quantum Transduction, and Institute for Sustainability and Energy at Northwestern, Northwestern University, Evanston, Illinois 60208-3113, United States; orcid.org/0000-0002-8761-7323; Email: mdkrzyaniak@northwestern.edu

Authors

Haochuan Mao — Department of Chemistry, Center for Molecular Quantum Transduction, and Institute for Sustainability and Energy at Northwestern, Northwestern University, Evanston, Illinois 60208-3113, United States; orcid.org/0000-0001-8742-089X

Gediminas J. Pažėra – Department of Chemistry, Center for Molecular Quantum Transduction, and Institute for Sustainability and Energy at Northwestern, Northwestern University, Evanston, Illinois 60208-3113, United States; Physical and Theoretical Chemistry Laboratory, Department of Chemistry, University of Oxford, Oxford OX1 3QZ, U.K.

Ryan M. Young — Department of Chemistry, Center for Molecular Quantum Transduction, and Institute for Sustainability and Energy at Northwestern, Northwestern University, Evanston, Illinois 60208-3113, United States; orcid.org/0000-0002-5108-0261

Complete contact information is available at: https://pubs.acs.org/10.1021/jacs.3c01243

Notes

The authors declare no competing financial interest.

ACKNOWLEDGMENTS

This work was supported by the National Science Foundation under award no. CHE-2154627 (M.R.W., synthesis, EPR measurements). The research was supported as part of the Center for Molecular Quantum Transduction, an Energy Frontier Research Center funded by the U.S. Department of Energy (DOE), Office of Science, Basic Energy Sciences (BES), under award #DE-SC0021314 (M.D.K., EPR data analysis). G.J.P. is grateful to the European Research Council (under the European Union's Horizon 2020 research and innovation program, Grant Agreement No. 810002, Synergy Grant: "QuantumBirds"). ¹H NMR spectroscopy and mass spectrometry were conducted in IMSERC facilities at Northwestern University, which have received support from the Soft and Hybrid Nanotechnology Experimental (SHyNE) Resource (NSF ECCS-2025633), NSF CHE-1048773, Northwestern University, the State of Illinois, and the International Institute for Nanotechnology (IIN).

REFERENCES

- (1) Harrow, A. W.; Montanaro, A. Quantum computational supremacy. *Nature* **2017**, *549*, 203–209.
- (2) Degen, C. L.; Reinhard, F.; Cappellaro, P. Quantum sensing. *Rev. Mod. Phys.* **2017**, *89*, 035002.
- (3) Biamonte, J.; Wittek, P.; Pancotti, N.; Rebentrost, P.; Wiebe, N.; Lloyd, S. Quantum machine learning. *Nature* **2017**, *549*, 195–202.
- (4) Wasielewski, M. R.; Forbes, M. D. E.; Frank, N. L.; Kowalski, K.; Scholes, G. D.; Yuen-Zhou, J.; Baldo, M. A.; Freedman, D. E.; Goldsmith, R. H.; Goodson, T.; Kirk, M. L.; McCusker, J. K.; Ogilvie, J. P.; Shultz, D. A.; Stoll, S.; Whaley, K. B. Exploiting chemistry and molecular systems for quantum information science. *Nat. Rev. Chem.* 2020, *4*, 490–504.
- (5) Atzori, M.; Sessoli, R. The second quantum revolution: Role and challenges of molecular chemistry. *J. Am. Chem. Soc.* **2019**, *141*, 11339–11352.
- (6) Troiani, F.; Affronte, M. Molecular spins for quantum information technologies. *Chem. Soc. Rev.* **2011**, *40*, 3119–3129.

- (7) Liu, Y.; Toma, F. M. Catalyst: Qubits from the bottom up. *Chem.* **2020**, *6*, 795–798.
- (8) Takui, T.; Berliner, L.; Hanson, G. Electron Spin Resonance (ESR) Based Quantum Computing; Springer: New York, 2016.
- (9) Sato, K.; Nakazawa, S.; Rahimi, R.; Ise, T.; Nishida, S.; Yoshino, T.; Mori, N.; Toyota, K.; Shiomi, D.; Yakiyama, Y.; Morita, Y.; Kitagawa, M.; Nakasuji, K.; Nakahara, M.; Hara, H.; Carl, P.; Hoefer, P.; Takui, T. Molecular electron-spin quantum computers and quantum information processing: Pulse-based electron magnetic resonance spin technology applied to matter spin-qubits. *J. Mater. Chem.* **2009**, *19*, 3739–3754.
- (10) Coronado, E. Molecular magnetism: From chemical design to spin control in molecules, materials and devices. *Nat. Rev. Mater.* **2020**, *5*, 87–104.
- (11) Nakazawa, S.; Nishida, S.; Ise, T.; Yoshino, T.; Mori, N.; Rahimi, R. D.; Sato, K.; Morita, Y.; Toyota, K.; Shiomi, D.; Kitagawa, M.; Hara, H.; Carl, P.; Hoefer, P.; Takui, T. A synthetic two-spin quantum bit: G-engineered exchange-coupled biradical designed for controlled-NOT gate operations. *Angew. Chem., Int. Ed.* **2012**, *51*, 9860–9864.
- (12) Rugg, B. K.; Krzyaniak, M. D.; Phelan, B. T.; Ratner, M. A.; Young, R. M.; Wasielewski, M. R. Photodriven quantum teleportation of an electron spin state in a covalent donor-acceptor-radical system. *Nat. Chem.* **2019**, *11*, 981–986.
- (13) Nelson, J. N.; Zhang, J.; Zhou, J.; Rugg, B. K.; Krzyaniak, M. D.; Wasielewski, M. R. CNOT gate operation on a photogenerated molecular electron spin-qubit pair. *J. Chem. Phys.* **2020**, *152*, 014503.
- (14) Olshansky, J. H.; Zhang, J.; Krzyaniak, M. D.; Lorenzo, E. R.; Wasielewski, M. R. Selectively addressable photogenerated spin qubit pairs in DNA hairpins. *J. Am. Chem. Soc.* **2020**, *142*, 3346–3350.
- (15) Aguila, D.; Barrios, L. A.; Velasco, V.; Roubeau, O.; Repolles, A.; Alonso, P. J.; Sese, J.; Teat, S. J.; Luis, F.; Aromi, G. Heterodimetallic [LnLn'] lanthanide complexes: Toward a chemical design of two-qubit molecular spin quantum gates. *J. Am. Chem. Soc.* **2014**, *136*, 14215–22.
- (16) Fernandez, A.; Moreno Pineda, E.; Muryn, C. A.; Sproules, S.; Moro, F.; Timco, G. A.; McInnes, E. J. L.; Winpenny, R. E. P. Gengineering in hybrid rotaxanes to create AB and AB₂ electron spin systems: EPR spectroscopic studies of weak interactions between dissimilar electron spin qubits. *Angew. Chem., Int. Ed.* **2015**, *54*, 10858–10861.
- (17) Zadrozny, J. M.; Niklas, J.; Poluektov, O. G.; Freedman, D. E. Millisecond coherence time in a tunable molecular electronic spin qubit. *ACS Cent. Sci.* **2015**, *1*, 488–492.
- (18) Zadrozny, J. M.; Gallagher, A. T.; Harris, T. D.; Freedman, D. E. A porous array of clock qubits. *J. Am. Chem. Soc.* **2017**, *139*, 7089–7094.
- (19) Atzori, M.; Chiesa, A.; Morra, E.; Chiesa, M.; Sorace, L.; Carretta, S.; Sessoli, R. A two-qubit molecular architecture for electron-mediated nuclear quantum simulation. *Chem. Sci.* **2018**, *9*, 6183–6192.
- (20) Bayliss, S. L.; Laorenza, D. W.; Mintun, P. J.; Kovos, B. D.; Freedman, D. E.; Awschalom, D. D. Optically addressable molecular spins for quantum information processing. *Science* **2020**, *370*, 1309–1312.
- (21) Lombardi, F.; Lodi, A.; Ma, J.; Liu, J.; Slota, M.; Narita, A.; Myers William, K.; Müllen, K.; Feng, X.; Bogani, L. Quantum units from the topological engineering of molecular graphenoids. *Science* **2019**, *366*, 1107–1110.
- (22) Shiddiq, M.; Komijani, D.; Duan, Y.; Gaita-Ariño, A.; Coronado, E.; Hill, S. Enhancing coherence in molecular spin qubits via atomic clock transitions. *Nature* **2016**, *531*, 348–351.
- (23) Yu, C.-J.; Krzyaniak, M. D.; Fataftah, M. S.; Wasielewski, M. R.; Freedman, D. E. A concentrated array of copper porphyrin candidate qubits. *Chem. Sci.* **2019**, *10*, 1702–1708.
- (24) Gaita-Ariño, A.; Luis, F.; Hill, S.; Coronado, E. Molecular spins for quantum computation. *Nat. Chem.* **2019**, *11*, 301–309.
- (25) Fernandez, A.; Ferrando-Soria, J.; Pineda, E. M.; Tuna, F.; Vitorica-Yrezabal, I. J.; Knappke, C.; Ujma, J.; Muryn, C. A.; Timco,

- G. A.; Barran, P. E.; Ardavan, A.; Winpenny, R. E. P. Making hybrid [n]-rotaxanes as supramolecular arrays of molecular electron spin qubits. *Nat. Commun.* **2016**, *7*, 10240.
- (26) Warren, S. W. The usefulness of NMR quantum computing. Science 1997, 277, 1688–1690.
- (27) DiVincenzo, D. P. The physical implementation of quantum computation. *Fortschr. Phys.* **2000**, *48*, 771–783.
- (28) Harvey, S. M.; Wasielewski, M. R. Photogenerated spin-correlated radical pairs: From photosynthetic energy transduction to quantum information science. *J. Am. Chem. Soc.* **2021**, *143*, 15508–15529
- (29) Laorenza, D. W.; Kairalapova, A.; Bayliss, S. L.; Goldzak, T.; Greene, S. M.; Weiss, L. R.; Deb, P.; Mintun, P. J.; Collins, K. A.; Awschalom, D. D.; Berkelbach, T. C.; Freedman, D. E. Tunable Cr⁴⁺ molecular color centers. *J. Am. Chem. Soc.* **2021**, *143*, 21350–21363.
- (30) Mani, T. Molecular qubits based on photogenerated spin-correlated radical pairs for quantum sensing. *Chem. Phys. Rev.* **2022**, *3*, 021301.
- (31) Closs, G. L.; Forbes, M. D. E.; Norris, J. R. Spin-polarized electron-paramagnetic resonance-spectra of radical pairs in micelles observation of electron spin-spin interactions. *J. Phys. Chem.* **1987**, *91*, 3592–3599.
- (32) Buckley, C. D.; Hunter, D. A.; Hore, P. J.; McLauchlan, K. A. Electron spin resonance of spin-correlated radical pairs. *Chem. Phys. Lett.* **1987**, 135, 307–312.
- (33) Bell, J. S. On the Einstein-Poldolsky-Rosen paradox. *Physics* **1964**, *1*, 195–200.
- (34) Thurnauer, M. C.; Norris, J. R. An electron spin echo phase shift observed in photosynthetic algae: Possible evidence for dynamic radical pair interactions. *Chem. Phys. Lett.* **1980**, *76*, 557–561.
- (35) Tang, J.; Norris, J. R. Theoretical calculations of microwave effects on the triplet yield in photosynthetic reaction centers. *Chem. Phys. Lett.* **1983**, *94*, 77–80.
- (36) Hore, P. J., Analysis of polarized electron paramagnetic resonance spectra. In *Advanced EPR in Biology and Biochemistry*; Hoff, A. J., Ed.; Elsevier: Amsterdam, 1989; pp 405–440.
- (37) Gierer, M.; Van der Est, A.; Stehlik, D. Transient EPR of weakly coupled spin-correlated radical pairs in photosynthetic reaction centers: Increased spectral resolution from nutation analysis. *Chem. Phys. Lett.* **1991**, *186*, 238–247.
- (38) Hoff, A. J.; Gast, P.; Dzuba, S. A.; Timmel, C. R.; Fursman, C. E.; Hore, P. J. The nuts and bolts of distance determination and zero-and double-quantum coherence in photoinduced radical pairs. *Spectrochim. Acta, Part A* 1998, 54A, 2283–2293.
- (39) Horwitz, N. E.; Phelan, B. T.; Nelson, J. N.; Mauck, C. M.; Krzyaniak, M. D.; Wasielewski, M. R. Spin polarization transfer from a photogenerated radical ion pair to a stable radical controlled by charge recombination. *J. Phys. Chem. A* **2017**, *121*, 4455–4463.
- (40) Horwitz, N. E.; Phelan, B. T.; Nelson, J. N.; Krzyaniak, M. D.; Wasielewski, M. R. Picosecond control of photogenerated radical pair lifetimes using a stable third radical. *J. Phys. Chem. A* **2016**, *120*, 2841–2853.
- (41) Colvin, M. T.; Carmieli, R.; Miura, T.; Richert, S.; Gardner, D. M.; Smeigh, A. L.; Dyar, S. M.; Conron, S. M.; Ratner, M. A.; Wasielewski, M. R. Electron spin polarization transfer from photogenerated spin-correlated radical pairs to a stable radical observer spin. *J. Phys. Chem. A* **2013**, *117*, 5314–5325.
- (42) Mi, Q.; Chernick, E. T.; McCamant, D. W.; Weiss, E. A.; Ratner, M. A.; Wasielewski, M. R. Spin dynamics of photogenerated triradicals in fixed distance electron donor-chromophore-acceptor-TEMPO molecules. *J. Phys. Chem. A* **2006**, *110*, 7323–7333.
- (43) Olshansky, J. H.; Harvey, S. M.; Pennel, M. L.; Krzyaniak, M. D.; Schaller, R. D.; Wasielewski, M. R. Using photoexcited core/shell quantum dots to spin polarize appended radical qubits. *J. Am. Chem. Soc.* **2020**, *142*, 13590–13597.
- (44) Nielsen, M. A.; Chuang, I. L. Quantum Computation and Quantum Information; Cambridge University Press: Cambridge, UK, 2000.

- (45) Christensen, J. A.; Zhang, J.; Zhou, J.; Nelson, J. N.; Wasielewski, M. R. Near-infrared excitation of the *peri*-xanthenoxanthene radical cation drives energy-demanding hole transfer reactions. *J. Phys. Chem. C* **2018**, *122*, 23364–23370.
- (46) Mao, H.; Young, R. M.; Krzyaniak, M. D.; Wasielewski, M. R. Controlling the dynamics of three electron spin qubits in a donor-acceptor-radical molecule using dielectric environment changes. *J. Phys. Chem. Lett.* **2021**, *12*, 2213–2218.
- (47) Greenfield, S. R.; Svec, W. A.; Gosztola, D.; Wasielewski, M. R. Multistep photochemical charge separation in rod-like molecules based on aromatic imides and diimides. *J. Am. Chem. Soc.* **1996**, *118*, 6767–6777.
- (48) Prato, M.; Maggini, M. Fulleropyrrolidines: A family of full-fledged fullerene derivatives. *Acc. Chem. Res.* **1998**, 31, 519–526.
- (49) Young, R. M.; Dyar, S. M.; Barnes, J. C.; Juricek, M.; Stoddart, J. F.; Co, D. T.; Wasielewski, M. R. Ultrafast conformational dynamics of electron transfer in exbox⁴⁺⊂perylene. *J. Phys. Chem. A* **2013**, *117*, 12438−12448.
- (50) Roy, I.; Bobbala, S.; Beldjoudi, Y.; Nguyen, M. T.; Young, R. M.; Cetin, M. M.; Cooper, J. A.; Allen, S.; Anamimoghadam, O.; Scott, E. A.; Wasielewski, M. R.; Stoddart, J. F. Supramolecular photoprotection of a photosensitizer for safe lysosomal delivery and regulated anticancer therapy. *J. Am. Chem. Soc.* **2019**, *141*, 12296–12304.
- (51) Stoll, S.; Schweiger, A. Easyspin, a comprehensive software package for spectral simulation and analysis in EPR. *J. Magn. Reson.* **2006**, *178*, 42–55.
- (52) Schweiger, A.; Jeschke, G. Principles of Pulse Electron Paramagnetic Resonance, 1st ed.; Oxford University Press, USA: Oxford, 2001.
- (53) Guldi, D. M.; Prato, M. Excited-state properties of C₆₀ fullerene derivatives. *Acc. Chem. Res.* **2000**, 33, 695–703.
- (54) Leach, S.; Vervloet, M.; Despres, A.; Breheret, E.; Hare, J. P.; Dennis, T. J.; Kroto, H. W.; Taylor, R.; Walton, D. R. M. Electronic spectra and transitions of the fullerene C₆₀. *Chem. Phys.* **1992**, *160*, 451–466.
- (55) Hore, P. J.; Hunter, D. A.; Mckie, C. D.; Hoff, A. J. Electron-paramagnetic resonance of spin-correlated radical pairs in photosynthetic reactions. *Chem. Phys. Lett.* **1987**, *137*, 495–500.
- (56) Bowman, M. K.; Maryasov, A. G. The direct dimension in pulse EPR. *Appl. Magn. Reson.* **2021**, *52*, 1041–1062.
- (57) Tang, J.; Thurnauer, M. C.; Norris, J. R. Electron spin echo envelope modulation due to exchange and dipolar interactions in a spin-correlated radical pair. *Chem. Phys. Lett.* **1994**, *219*, 283–290.
- (58) Volkov, M. Y.; Salikhov, K. M. Pulse protocols for quantum computing with electron spins as qubits. *Appl. Magn. Reson.* **2011**, *41*, 145–154.
- (59) Salikhov, K. M.; Kandrashkin, Y. E.; Salikhov, A. K. Peculiarities of free induction and primary spin echo signals for spin-correlated radical pairs. *Appl. Magn. Reson.* **1992**, *3*, 199–216.
- (60) Dzuba, S. A.; Gast, P.; Hoff, A. J. ESEEM study of spin-spin interactions in spin-polarized P⁺Q_a⁻ pairs in the photosynthetic purple bacterium *Rhodobacter sphaeroides* R26. *Chem. Phys. Lett.* **1995**, 236, 595–602.
- (61) Long, G. L.; Yan, H. Y.; Yang, S. Analysis of density matrix reconstruction in NMR quantum computing. *J. Opt. B* **2001**, *3*, 376. (62) Lee, J.-S. The quantum state tomography on an NMR system. *Phys. Lett. A* **2002**, *305*, 349–353.